Quantitative tomography of hydrogen precharged and uncharged Al-Zn-Mg-Cu alloy after tensile fracture

Gupta, Chiradeep
Department of Mechanical Engineering, Toyohashi University of Technology

Toda, Hiroyuki
Department of Mechanical Engineering, Kyushu University

Fujioka, T.
Department of Mechanical Engineering, Toyohashi University of Technology

Kobayashi, Masakazu
Department of Mechanical Engineering, Toyohashi University of Technology

他

出版情報：Materials Science and Engineering : A. 670, pp.300-313, 2016-07-18. Elsevier
バージョン：
権利関係：

Quantitative tomography of hydrogen precharged and uncharged Al-Zn-Mg-Cu alloy after tensile fracture

C. Gupta[1, a], H. Toda[1,b], T. Fujioka[1], M. Kobayashi[1], H. Hoshino, K. Uesugi[2], A. Takeuchi[2], Y. Suzuki[2]

1: Department of Mechanical Engineering, Toyohashi University of Technology, Toyohashi, Aichi 441-8150, Japan.

2: Japan Synchrotron Radiation Institute, Sayo-Gun, Hyogo, Japan.

a: Presently at Materials Group, Bhabha Atomic Research Centre, Mumbai, India.

b: Presently at Department of Mechanical Engineering, Kyushu University, Japan.

Email : joy_gupta71@yahoo.co.in; cgupta@barc.gov.in

Abstract

Quantitative tomography is carried out on datasets derived from tensile fracture sample of electrochemically precharged Al-Zn-Mg-Cu alloy in the underaged condition and its uncharged counterpart. It is shown that precharging which induces a transition of tensile fracture mode from ductile to brittle, results in a significant increase in micro-damage content in the regions near the fracture surfaces. Using quantitative tomography analysis based on spatial mapping of morphologically segmented micro-damage content of the datasets it is found that the precharged sample contains an inhomogenous distribution of micro-pores near grain boundaries. It is also shown that the spatial architecture of micro-pores in the dataset is not influenced by the plastic zone of the intergranular cracks lying along the grain boundaries. Contrastingly the micro-pores in the tomographic dataset of the uncharged sample are shown to be present near intermetallic particles. It is therefore rationalized that the spatial architecture of micro-pores in the datasets from uncharged sample originate from particle cracking during ductile fracture, and from the tendency for damage enhancement by the synergism of hydrogen exposure near grain boundaries and localization of deformation in the precharged sample dataset.

1 Introduction

The manifestations of hydrogen embrittlement failure in materials can vary from inter-granular cracking to ductile micro void coalescence (with reduced dimple size) [1 - 3]. Inter-granular cracking is a particularly insidious manifestation of the deleterious effect that hydrogen has on the fracture behavior of varieties of high strength aluminum alloys [4, 5]. However, this hydrogen induced cracking effect is largely restricted to the high strength aluminum alloys such as Al-Mg, Al-Zn-Mg, Al-Zn-Mg-Cu [6]. As high strength aluminum alloys find applications as structural material in technologically intensive industries [4] (eg. aerospace, oil and hydrogen storage), considerable scientific effort has been devoted to clarify the causative and mitigating factors responsible for hydrogen induced cracking in aluminum alloys. The plausible causes for the adverse impact of hydrogen that pre-dispose the grain boundaries in aluminum alloys to form cracks are due to the presence of grain boundary precipitates (eg. $MgZn_2$:η precipitates in AA7075) above a certain size [7,8], that trap the hydrogen, or to the formation and segregation of Mg-H complexes [9] or to the presence of bubbles [10].The microstructural factors attributed to promote the grain boundary cracking range from type and coherency of precipitates, solute segregation at grain boundaries, precipitate free zones, grain texture etc [11-14]. Thus, not only the manifestations of hydrogen led degradation are multifarious but there is also an enormous diversity in the attributable factors for promoting hydrogen embrittlement in aluminum alloys. The scientific challenge to mechanistically reconcile the wide disparity in the manifestation of hydrogen embrittlement in aluminum alloys with the multitude of causative factors still remains quite daunting.

The ingress of hydrogen via electrochemical charging at high fugacities is commonly known to create damage in matrix of materials [6,15]. The most pernicious effect of hydrogen embrittlement is through the propagation of intergranular crack which has its origins at the micro-meter scale. It is to be expected that the formation of micro-meter scale damage structures are likely to be influenced by the presence of matrix defects such as vacancies and dislocations. In aluminum, the nature of matrix damage has been investigated using techniques such as SANS and SAXS which revealed that the constituents of sub-micrometer scale defects consists of vacancy clusters, micro-voids, and dislocations [16-17]. In regards to investigating the damage as result of degradation phenomenon such as corrosion, the microtomography technique is most suitable. The intrinsic advantages of the tomography technique at large synchrotron sources, providing 3D internal volumetric images with high spatial and density

resolution in a non-destructive manner makes it an apt tool to study the internal damage caused by the corrosion process. As a result in recent years there is growing interest in studying the corrosion phenomena in materials by microtomography using ex-situ and in-situ methods [18 -21]. Eckerman et.al [18] investigated the susceptibility of the AlMgSi alloys containing surface deformed layer to localized corrosion attack immersed in HCl solution of lean and concentrated strengths. Conolly et. al. [19] showed inter-granular path propagation and dissolution of the matrix around inter-metallic particles using in-situ micro-tomography. Knight, Davenport and co-workers [20] used the high density resolution feature from synchrotron micro-tomography provided by high mono-chromaticity of the beam to characterize the initiation and propagation of intergranular cracking in high strength aluminum alloys. They also used synchrotron micro-tomography in an in-situ mode to characterize the development of pitting corrosion in stainless steel [21]. More recently Singh et. al. [22, 23] studied the corrosion behavior with time and cracking behavior under stress using in-situ experiments on high strength aluminum alloy. As the effects of corrosion are time dependent, in-situ microtomography technique was applied to monitor the crack growth during corrosion - fatigue phenomenon in AA 7075 [24]. The microtomography technique is also being used in combination with other experimental techniques relevant in the context of corrosion such as nanoindentation and thermal desorption spectroscopy (TDS) to reveal new quantitative correlations between extent of degradation and change in microstructure [25, 26].

In the understanding of hydrogen embrittlement the knowledge of spatial distribution of hydrogen in the matrix is quite valuable. A technique to map the distribution of hydrogen in structural materials such as iron and aluminum alloys is neutron tomography. The neutron tomography studies carried out on ARMCO iron using experimental setup having a spatial resolution of 25μm, shows that the hydrogen distribution near regions of cracks and blisters formed by electro-chemical charging is significantly enhanced [27]. Similar observations were made in Al by Hoshihira et. al. [28].Complementary 2D EBSD studies to the neutron tomography scans showed that numerous micro-pores were in close vicinity to the inter-granular cracks and therefore were interpreted to be precursors to these cracks. The propensity of different types of sites in AA 7150 to trap hydrogen has been recently shown by the application of micro-tomography and TDS technique thereby extending the analysis to include microstructural (eg. solutes, grain boundaries), micro-pore and matrix defect sites (vacancies and dislocations) [26]. Such analysis should reveal the most likely site contributing to hydrogen

embrittlement in materials especially for Al-Zn-Mg-Cu alloys distinguished by high diversity of trapping sites.

There is, thus, evidence to relate the presence of different types of matrix defects that can act as portent hydrogen traps [29]. This implies that mapping of the concurrent damage occurring with hydrogen ingress and redistribution by deformation could be important for providing new insights on mechanisms of embrittlement. However, there is no study that relates the tendency of high fugacity hydrogen charging that enhances matrix damage in materials [30] and, the manifestation of hydrogen embrittlement by a change in failure mode. Therefore in this study the micro-damage architecture in sample coupons of a high strength aluminum alloy Al-Zn-Mg-Cu type is studied using synchrotron microtomography (SR-μCT) with the aim of relating it to the fracture mode transition obtained by precharging a tensile sample. For this purpose the state of the art approach of quantitative tomography [31] is applied. Quantitative tomography uses high fidelity tomographic images for revealing the mechanistic underpinnings of damage development due to degradation phenomena and material microstructure based on correlative parameters [32, 33]. The quantitative tomography analysis in this work is directed to reveal the importance of grain boundary and intermetallic particles that are known to act as prominent hydrogen traps [26] in the development of the micro-damage architecture present in an Al-Zn-Mg-Cu alloy after ductile and hydrogen induced brittle failure.

2 Experimental

2.1 Materials

The high strength aluminum alloy, that that has been selected for the studies is AA 7075. The chemical composition of the alloy is given in table 1. It was received as hot extruded rods with typical flat pancake grain structure. The material was heat treated by a solutioning step at 520°C for 144 hours followed by aging at 120°C for 8 hours in an oil bath. This long solutioning treatment transformed the flat pancake grain structure found in the hot extruded rods of AA7075 to an equi-axed microstructure with average grain size of about 80μm. Linear intercept method was used to estimate the average grain size. The underaging treatment was carried out as it is well known that this treatment is most susceptible to hydrogen embrittlement in AA7075 alloy [34].

2.2 Hydrogen Charging

The electrochemical method was used to charge hydrogen in the machined cylindrical tensile sample. The setup consisted of poisoned sulphuric acid of 0.5 M strength as electrolyte. A fine platinum wire mesh acted as the anode and the tensile sample was the cathode. These

were connected to a constant DC power source by platinum wires. The samples were charged using a current density of 4000 A/m^2 for 72 hours with continuous stirring of the electrolyte. Prior to charging, small coupons of AA7075 were exposed to the same heat treatment as the tensile samples. These were charged simultaneously with the tensile sample in the electrochemical cell. Subsequently the samples were analyzed by vacuum fusion method to assess the total hydrogen content. It was found that the total hydrogen content increased from 0.18 ml H/100 Al to 0.82 ml H/100 g Al as a result of the cathodic charging.

2.3 Tensile Tests

The tensile test was carried out using a screw driven universal testing machine at room temperature using a nominal strain rate of 10^{-6} s^{-1} using cylindrical samples of 6 mm diameter and 30 mm gauge length on charged and uncharged specimens (sketch in fig. 1(a)). The nominal displacement rate for achieving the prescribed strain rate was 1.8μm/min. The tensile tests on specimens pre-exposed to hydrogen were carried out within a few hours of the charging step. The load, displacement and strain data were recorded during the test. The strain was measured using a laser extensometer that scanned between two markers placed 5 mm apart in the central portion of gauge section of the specimen corresponding to its viewing window. During testing, the humidity in the air was kept in the range 65 ± 5 %R.H. The load – displacement data was converted to stress-strain plot using standard formula. The fracture surfaces of the broken specimens were observed in a JEOL make SEM operating at 10 kV to assess the nature of failure.

2.4 Synchrotron Micro-tomography Imaging (SR-μCT)

The micro-tomography scans were carried out at the BL20XU beam line at SPring-8 on various sample coupons extracted from tensile specimens. In order to extract the sample coupons, firstly fracture surface of the broken halves of the tensile specimen was covered by cold mounting. Fine precision slicing using slow cut parallel to the load axis of the sample was then applied to generate the coupon containing the surface of the tested specimen. The coupon was then mounted using a double sided tape and manually ground on a 1200 grit paper. The grinding was periodically interrupted to measure the extent of thickness reduced on the opposite and transverse sides to the external surface, until a regular cross-section of nearly 0.6 x 0.6 mm^2 was achieved. The sample coupon thus prepared was cut to a length of 10 mm. The region selected in both tensile tested specimens is near its outer diameter surface and also contains the fracture surface. This ensures the regions of the precharged specimen considered

for scanning have adequate exposure to hydrogen during charging and in the subsequent deformation. The various stages for preparing the sample coupons used to tomographic scanning from the tested tensile specimens are shown in figure 2. Furthermore selecting regions that are near the outer surface will minimize the influence of necking on the development of micro-damage while undergoing ductile or brittle fracture.

The sample coupon of size 0.6x0.6x10 mm^3 was scanned in the micro-tomography set-up at un-dulator beam line BL20XU consisting of a liquid nitrogen cooled double crystal mono-chromator (Si (111)-(111)), diffuser, and a pair of orthogonal slits. A monochromatic beam of energy 20 keV illuminated the sample placed on a precision rotation stage. The projection data recorded by an image detector system, placed 55 mm from the sample, consisting of a cooled 4000 (H) × 2624 (V) element CCD camera (effective pixel size of the camera: 5.9 µm, used in 2 x 2 binning mode), a LSO:Ce scintillator (Lu_2SiO_5:Ce) and a relay lens (×20). In total, 1500 radiographs, scanning 180 degrees, were obtained in 0.12-degree increments. The exposure time for a single shot was 30 ms. The resolution limit (the theoretical lower bound of which is governed by the Rayleigh criterion for diffraction, that is estimated to be ~ 750nm for the set-up) of this projection-type SR-µCT set-up is approximately 1 µm, which is determined primarily by image blurring caused by the Fresnel diffraction, the diffraction limit of visible light and the spatial resolution of a scintillator [35]. Isotropic voxels (a volume element in 3D space) with 0.5 µm edges were achieved in the reconstructed slices that were at least necessary to achieve the 1 µm spatial resolution [36]. A convolution back projection algorithm was used for achieving the reconstruction into 16 bit slice dataset. For the purpose of quantitative analysis these 16 bit slice dataset were converted into 8 bit gray scale slice dataset by mapping the linear attenuation coefficient in the range 0 – 40 cm^{-1}. The volume rendering in 3D of the 8 bit reconstructed images obtained from the micro-tomography scans and its subsequent processing was carried out using VGSTUDIO MAX. The quantitative analysis of the dataset has been carried out by custom software that implemented the marching cube algorithm. The features of each of the objects such as volume, surface area and sphericity along with its center of mass have been evaluated in the region of interest.

2.5 Quantitative Tomography

The quantitative analysis of the dataset has been carried out by custom software that implemented the marching cube algorithm. The features of each of the objects such as volume,

surface area and sphericity along with its centre of mass have been evaluated in the region of interest. These quantitative data have been used to calculate the following 3D characteristics attributable to the class of object visualized in the volume.

$$V_f = V/V_{Al} \quad (1)$$

$$d = 2\sqrt[3]{3V/4\pi} \quad (2)$$

$$S_p = \sqrt[3]{36\pi V^2}/A_p \quad (3)$$

$$\rho_p = n/V_{Al} \quad (4)$$

Where V_f = volume fraction of the object; V = volume of the voids; V_{Al} = volume of the aluminum alloy matrix; d = void diameter; S_P = Sphericity; A_p = surface area of the void; ρ_P= number density; n = number of voids in the region of interest.

The damage characterized in the two datasets were morphologically classified according to a damage morphological parameter (DMP) as per the following expression:

$$DMP = 10 \log_{10}\left(\frac{\xi_{ideal}}{\xi_{actual}}\right) \quad (5)$$

where, ξ_{ideal}= volume to surface area of ideal sphere of given size, ξ_{actual} = actual volume to surface area of the damage of the same given size.

The morphological expression classifies the damage object on the basis of its given size derived from the quantification of its volume in the tomography dataset. Subsequently a DMP value denoting the object shape is provided by comparing volume to surface area of the corresponding volume equivalent sphere to the actual values of these quantified parameters in the tomography dataset. This approach to compute the DMP provides a conservative approach to distinguish between pores and cracks over a wide size range. The basic criterion used in the study to classify cracks from pores present in the various datasets is fixed to have at least DMP value of 7. This DMP value is used as it implies that the cracks have an actual volume to area ratio one fifth that of its idealized sphere, which is similar to the approach adopted by Williams et. al. [37] on the basis of minimum and maximum dimensions of the sphere fitted to the given damage contained in ceramics. Furthermore the morphology of the pores is classified as ellipsoid or acicular based on a respective DMP value greater or less than 2.5. Using DMP as the morphological parameter and damage size (ϕ), the micro-damage content is further

subdivided into micro-pore (small and large ellipsoidal : μE:sPore ((DMP, ϕ) ≡ (<2.5,<8 μm)) &μE:LPore ((DMP, ϕ) ≡ (<2.5,8-18 μm)); small and large acicular : μA:sPore ((DMP, ϕ) ≡ (2.5-7,<8 μm)) &μA:LPore ((DMP, ϕ) ≡ (2.5-7,8-18 μm))) as well as micro-cracks (small : μs:Crack ((DMP, ϕ) ≡ (>7,<8 μm)) ; large : μL:Crack ((DMP, ϕ) ≡ (>7,8-18 μm)) and very large : μXL:Crack ((DMP, ϕ) ≡ (>7,>18 μm))) in the two datasets.

An analysis of the micro-pore clustering near the cracks could provide an indication of the microstructural origin of the spatial heterogeneity of the micro-damage architecture observed in the sample that failed in an intergranular fashion. Once the radial distribution of the micro-pore occurrence probability is determined it is possible to determine the pattern of radial distribution around the intergranular cracks from the clustering plots. One way to characterize the agglomerating tendency is to analyze the frequency of clustering of the micro-pores as described by the variation in occurrence of peaks of RPP parameter (given in Appendix-A) as a function of radial distance from the crack. The following clustering parameter in the two datasets has been defined to analyze the clustering of peaks seen in the radial variation of RPP. This parameter denoted as β defined for a sampling length ρ_L along the radial distance from the crack centre and is based on counting the number of RPP peaks ($n(\rho_L)$) and computing their average separation ($\bar{\Delta}$) occurring within ρ_L. The expression is given below:

$$\beta = \frac{\rho_L}{n(\rho_L)} \frac{1}{\bar{\Delta}} \qquad (6)$$

The parameter β defined as above is the ratio of the uniform peak separation to its average actual value within a sampling length ρ_L. Hence a value of $\beta > 1$ indicates that peaks within the sampling length are clustered and $\beta \leq 1$ indicates that the peaks are either uniformly distributed or have a spacing wider than that of the uniform distribution of peaks within ρ_L.

3. Results

3.1 Tensile Testing

The flow behavior from the tensile test of hydrogen pre-charged and uncharged AA7075 is shown in figure 3. The influence of the charging on the tensile behavior is clearly manifested by a lowering of both the flow stress and decrease in ductility. The fracture strain for the un-charged specimen is seen to be about ~ 0.15 or about three times that of the hydrogen pre-charged specimen. It is clearly seen that there is hardly any necking behavior (i.e. a significant decrease in stress before fracture) displayed in the tensile flow curve for the hydrogen pre-charged case as compared with the uncharged sample. The fracture surface shown in figure

4(a) is typical of intergranular failure clearly showing faceted grain features. There are, however, few areas where ductile dimples are also evident. The samples that were tested in tension after hydrogen pre-charging were distinguished by the presence of intergranular cracks emanating from outside surface and oriented perpendicular to the load axis. This is likely as the concentration of hydrogen after pre-charging is expected to be highest at below the outer surface. Furthermore an underage heat treatment has been provided that makes the aluminum alloy susceptible to intergranular failure cracking along grain boundaries at the surface. An example of this is shown in figure 4(b). Such cracks were absent in the tensile tested samples of AA 7075 which were not electrochemically charged. The fracture surface of the uncharged tensile sample is shown in figure 4(c). The presence of extensive dimples provides evidence that the failure has been ductile in nature. The fractograph also contains areas with shallow dimpled structure, giving appearance of being featureless. These could be areas where the hydrogen content could be enhanced due to matrix trapping or ingress from humid air during the test. However, in comparison with the precharged sample, where the failed surface shows predominantly intergranular fracture characteristics, for the uncharged tensile sample the fracture is considered to be ductile in nature.

The regions close to the surface after failure in the broken sample were further investigated using microtomography scanning. The scans enabled characterization of the micro-damage architecture for the H-charged specimen failed by intergranular mechanism and H free specimen that failed by ductile mechanism. This evaluation of the damage state in fracture samples of the two specimens implies a comparison at two different strains. Despite this apparent strain dependency of the observations, the study using failed samples were considered to be adequate for the aims of the investigation as they represented the characteristic deformation before cataclysmic fracture for two different modes of failure (brittle intergranular verses ductile fracture) for the underaged AA7075.

3.2 3D Visualization.

Typical 2D slices in the dataset used for 3D visualization obtained from tomography of sample coupon exposed to hydrogen are shown in figure 5 (a) and (b) corresponding to two regions in the scanned volume. Figure 5(c) also shows a typical slice obtained from the tomographic scan of uncharged sample coupon. Numerous black areas of different sizes embedded in a gray matrix can be seen which collectively form the damage content in the hydrogen exposed region of the sample in figure 5(a) and (b). The black regions especially the smaller ones are taken as micro-damage as they occur with their edges having bright contrast.

The two slices contained large black regions that clearly correspond to two regions in the dataset: one containing a large crack that extends over multiple grain boundaries and the other containing much smaller cracks of sizes ranging from one to two grain boundaries. The presence of micro-pore can also be clearly seen in both slices. The surrounding Al matrix is seen as gray. The bright circular shaped objects in the slices are intermetallic particles (containing Fe, Cu and Al) typically found in the AA7075. These particles are seen in the slices to be oriented along the original extrusion direction. The dark region outside the boundaries of the gray Al-matrix is simply air. The presence of Mg_2Si particles are not considered in the matrix of the samples of equi-axed underaged 7075 used for the study. This is because of the long solutioning temperatures above 500°C given to obtain an equi-axed microstructure of the 7075 grade alloy. At these temperatures the Mg_2Si particles are reported to dissolve in minutes [38]. In a recent study the particles were imaged using SR-μCT in an underaged 7075 that was given short term solutioning at temperatures below 500°C [25]. In the tomographic dataset, obtained from scanning an undeformed sample of underaged 7075, the particles were considered to be Mg_2Si as those that appeared as irregular shaped with gray regions without edge enhance contrast [25]. It is to be mentioned here that apart from the inter-metallic particles typically the underaged microstructure also has sub-micrometer particles typically of $MgZn_2$ type. Nguyen et. al. [39] clarified the role of these particles in causing intergranular fracture in underaged AA7075. However the studies by Toda et. al. [40, 41] and Gupta et. al. [42] shows that formation of hydrogen micro-pores is predominately influenced by the intermetallic particles. Hence sub-micrometer characterization of the particles was not carried out. In figure 5(c) the typical slice shows a fracture surface that is tilted with respect to the loading axis (which is in the vertical direction). Contrastingly a nearly flat fracture surface is seen in figure 5(a) corresponding to the slice from the hydrogen exposed sample coupon. In the uncharged sample coupon, figure 5(c), the slice also shows that the particles are cracked.

The 3D visualization of the datasets is shown in figure 6. In figure 6(a) the visualization of the scan volume is depicted in 3D with and without segmentation. The volume with segmentation clearly shows the arrangement of the penetrative intergranular crack (yellow) with the pores (red) and particles (Aqua/teal). The volume without segmentation is shown in gray where it can be seen that the intergranular crack originates at the surface. The penetrative intergranular crack has two parts clearly seen in the fig 6 (a). One part starts from surface and penetrates the bulk traversing many grains perpendicular to the Z-axis. A second part of the intergranular crack lies nearly parallel to the Z-axis, which represents the change of

direction a portion of the crack front as it connects to the fracture surface. The fig 6 (b) shows a close up view of the dataset near the large crack. It is seen that there are micro-pores and various types of smaller cracks within the matrix that also have an intergranular character. Thus three types of micro-damage can be distinguished – a single penetrative surface intergranular crack that extends over many grain boundaries, few short cracks extending not more than couple of grains which are either closed or open and, a large number of micro-pores (that are isolated or clustered). These different types of damage are morphologically distinguished using the DMP parameter.

In order to determine whether the micro-damage has a role to promote the propensity for intergranular cracking, it is essential to compare its spatial distribution in two volumes: one that contains the crack and the other that does not contain it. A straightforward way fulfill this requirement in the present study is to divide the scanned dataset into *two sub-regions*, one that contains the penetrative intergranular crack while the other does not contain it. The dataset obtained from the scans on sample coupon extracted from the intergranularly failed tensile specimen is therefore divided into two regions – one containing the large intergranular crack and the other volume relatively free of them. These two regions are compared with the dataset not electrochemically pre-charged with hydrogen. The region A is shown in the fig. 6 (b), which contains the intergranular crack. The 3D visualization of the dataset of the uncharged sample failed in typical shear failure is shown in fig. 6 (c). It is seen that the micro-damage consists only of the presence of pores (shown in red). The clustering of the micro-pores is seen to be absent as also the presence of intergranular crack.

3.3 Quantitative analysis and Micro-pore spatial architecture

The quantitative analyses of the two sub-regions A and B and the dataset of uncharged sample in terms of the change in 3D characteristics of micro-damage and particles such as volume fraction, size, number density and sphericity are compared in table 2. It is seen that the particle characteristics in the two regions are quite similar in terms of volume fraction, number density and size. However, the *micro-damage* content distributed in the respective regions is significantly different. The volume fraction of *micro-damage* is significantly higher in region A as compared with that in region B. Furthermore the number density is more and average size is larger in the region A as compared with that in region B. In keeping with the higher number density the inter-pore distance is smaller in region A as compared with region B. These trends suggest that in the region where inter-granular cracks are present the damage content is also

larger. In case of the sample coupon extracted from uncharged tensile specimen the quantitative analysis of the tomographic dataset reveals that micro-damage content is lower than that obtained by combining sub-volume region A and B. It can thus be concluded that the precharged tensile sample that displayed brittle fracture (region A and B) contains significantly greater micro-damage content as compared the sample failed in a ductile manner.

The micro-pores are segmented out from the micro-damage quantified using tomography in the respective datasets by placing an upper limit on size and morphology characteristics at a value of 8 μm and 7 respectively. These values have been chosen as per the criteria adopted in the previous work by the authors [43]. In terms of the number of micro-damage characterized more than 97% of the damage have been classified as micro-pores using these upper limit values of size and morphology in the respective datasets. The spatial architecture of the segmented out micro-pores from the micro-damage dataset are then depicted in terms of their distribution using image intensity maps that plot their number in local unit volumes. In order to construct the image intensity maps the coronal slices of the regions A and B have been divided equally into zones of 20 x 20 μm^2 and length equal to the respective region thickness. The number of pores in each of the zone is mapped and represented in the image intensity format. The fig. 7 shows a comparison between the spatial intensity map of the micro-pores in the region-A and -B. The intensity range in region A and B corresponds to micro-pore number range of 1 – 9 and 1 – 7 respectively in each of the sub-volumes. It is clearly seen that in region-A, three zones can be identified that contain cluster of sub-volumes with high number of micro-pores in close proximity to each other. These have been demarcated in the fig. 7(a) and can be considered as an agglomerated region where the large number of micro-damage occurs in close proximity. A visual comparison with the slice of region-A shown in figure 5(a) reveals that the identified agglomerated zones are near the location of intergranular cracks. In fact for the large intergranular crack extending many grains the corresponding agglomerated zone is also most extensive. In contrast in fig. 5(b) region-B which did not contain large penetrative intergranular crack such agglomerated zone is evidently absent and clustering is limited to a few dispersed local volumes containing high number of micro-pores. Similar trends were also reported near cracks linked underneath the hydrogen induced intergranular fracture surface of underage 7075 [43]. The trends show that the hydrogen induced intergranular crack penetrating into the bulk has an associated agglomerated zone where the *micro-pore* number is high.

The proximal relationship of the pores with particles is analyzed with the approach adopted earlier by the authors to provide an insight of the micro-pore formation in hydrogen

exposed AA7075 [42]. This relation between the pores and particles have been explored by calculating the ratio of the pore number and the particle number found in each zone and is denoted as the γ-parameter. A value of the parameter greater than 1 denotes a pore dominated zone, which in the image intensity format is displayed as higher gray scale intensity values. The distribution of the γ-parameter is compared with the particle distribution in the zones in the image intensity format so that the proximity of the pore dominated regions with the particle dominated regions in the dataset could be visualized. For this purpose a synthesis of a composite spatial intensity image map has been constructed by overlaying the particle number distribution intensity map with that of the γ-parameter distribution image intensity map. The results are shown in figure 8 for the two regions A and B and the uncharged specimen dataset. For the region A it is seen that the zone cluster with high number particles can be easily distinguished, while in region B there is no significant zone clustering (fig 8 (a, d)). On overlaying the γ-parameter distribution image intensity map over the corresponding particle number distribution in unit zones, it is seen that in case of region A the zone clusters of the γ-parameter are predominately near the zone clusters for the particles. In region B where there are no zone particle clusters, the γ-parameter zones are fairly evenly distributed. In both regions there is no significant overlap seen in the composite intensity maps of the particle distribution and γ-parameter. In contrast, in case of the uncharged specimen dataset the composite overlay of the γ-parameter over the particle spatial distribution in intensity map format shows significant overlap between the two.

The radial distance from the crack centre where the RPP (Appendix A) has been computed for the distribution of the micro-pore in the dataset can be divided into contiguous units equal to the sampling length and hence variation of the clustering parameter β may be determined along the radial length. Thus a plot of clustering parameter β as function of the radial length can be constructed which can reveal the influence of the grain boundaries to cluster the micro-pores. This is because such a condition would render the spatial interval for peak value of β to be in integral multiples of grain size. The plot of radial dependence of β for each crack found in the respective datasets is evaluated in terms of volume of the crack in a 3D plot format. The 3D plot for the dataset containing the integranular and ductile fracture surface is shown in fig. 9. A dramatic difference in the propensity for clustering of micro-pore is seen in the two datasets. The clustering effect that manifests as an undulating variation in the β-parameter in the Z – axis is quite prominent for the intergranularly failed sample as compared with the

specimen failed in a ductile manner. The wavelength of the undulation of the β parameter is between 75 – 85 μm which is close to the average grain size of the AA 7075 used for the study.

3.4 Crack tip plasticity and hydrogen induced Micro-damage distribution

The intergranular crack exerts a tri-axial field within its immediate vicinity. The effect of this zone has been predicted to promote the hydrogen redistribution at the elastic – plastic boundary. This has been quantitatively shown by Yokobori et. al. [44, 45] by analytically computing the stress gradient, using an estimation of the plastic zone size based on a slip field solution obtained by Hills analysis. Other researchers have pointed that the maximum hydrogen concentration would be at the interface of maximum hydrostatic stress that lies well within the plastic zone [46], typically at about 1.5 times the crack tip opening displacement. As the elastic plastic boundary is much larger in size than the interface of the maximum hydrostatic stress, the influence of the tri-axiality of the crack on the micro-damage formation would be indicated if they are within the plastic enclave ahead of the tip. In order to assess if the micro-damage observed in the present case is influenced by a stress induced redistribution of hydrogen a conservative estimate of the plastic zone size using the equation used by the Yokobori et. al. [45] has been adopted which estimates the location of the elastic-plastic boundary. The expression to estimate the plastic zone and the stress is as given below [45]:

$$r_p = \frac{1}{4\pi}\left(\frac{K_I}{\sigma_{ys}}\right)^2 \left[(1-2\nu)^2(1+cos\theta) + \left(\frac{3}{2}\right) sin^2\theta\right] \quad (7)$$

$$\sigma_P = \frac{2}{3}\,\alpha\,(1+\nu)\sigma_{ys}\left[\frac{1}{2} + \ln\left(\frac{r_p}{\rho}\right)\right] cos\frac{\theta}{2} \quad (8)$$

where, r_p = plastic zone size; σ_p = plastic stress; K_I = stress intensity factor ($=\alpha\sigma_o\sqrt{\pi a}$); σ_o = applied stress; σ_{ys} = Yield stress; ν = poisons ratio, θ = angle measured from the crack plane; ρ = crack tip radius, a = crack length, α = geometric factor (f (a/W)).

As compared with the diameter (D) of 6 mm of the sample, the a/D< 0.1 (where a = crack length) and for such short cracks embedded in a cylinder the f(a/W) ~ 1. As a first approximation, by considering the crack length to be the crack tip distance from the surface, the applied stress intensity at failure stress of 550 MPa is about 17 MPa.$m^{0.5}$. The plastic zone shape along with the stress depicted in the intensity format is super-imposed on the tomography slice that has been binarized and represented in false color, as shown in the enlarged region near the crack at a depth of 125μm from the surface in figure 10. This has been carried out on

all the slices containing the intergranular crack. The location of the micro-damage that has been found to be in the vicinity of the intergranular crack within these slice set has been plotted in the scatter diagram shown in figure 11. The plastic zone size region along the crack front is also shown in blue. It can be clearly seen that the majority of the micro-damage location lies outside the plastic zone size region. In order to quantify the fraction of the micro-damage that lies within and outside the plastic zone of the crack tip, the spatial location of both from the crack tip in cylindrical format were used to compute the respective number of pores in 2π. The results are shown in fig. 12. It is seen from fig. 12(a) that the pore number increases from one end of the crack front to the other. Significantly the fraction of pores within the plastic zone size is only 20% as compared with about 80% outside it. The fig. 12(b) shows the fraction of pores lying in a particular direction with respect to the crack tip. It is seen that fraction of the pore in the direction 240-300° is consistently near 40% along the crack front. In combination with those lying in the 180-240° direction (which is about 15-20%), it can be concluded that the majority of the pores lie in 180-300° direction to the crack tip. The circle area marked as yellow in the fig. 12 (b) is shown to clarify the direction of evaluation of the micro-damage content with respect to the crack tip. The lack of a significant fraction of micro-damage within the volume of crack tip plastic zone clearly shows that it exerts a weak influence on its development.

3 Discussion

The micro-damage characteristics contained in the sample coupons extracted from tensile specimens with hydrogen pre-exposure were compared with those that were contained in un-exposed specimens. The comparison of the micro-damage in individual datasets contained within regions underneath the respective fracture surfaces after tensile test can be summarized as follows:

1. The 3D rendering of the datasets revealed the presence of a surface connected intergranular crack with a tortuous morphology extending hundreds of micro-meters inside the specimen of the charged sample coupon.
2. The micro-damage content in sample displaying brittle mode of fracture is larger than that showing ductile fracture.
3. The micro-pore morphology also varied quite significantly within regions close to fracture surface displaying brittle and ductile mode of failure.
4. The proximity relationship of micro-pore and particles showed that pore rich regions overlapped with the particle rich regions for the specimen displaying ductile failure.

The region originating from embrittled specimen, however, did not display such overlap of the micro-pores.

5. The majority of micro-pores in the dataset obtained by scanning the coupon extracted from specimen displaying brittle fracture are distributed outside the plastic zone region of the large intergranular crack connected to the surface.
6. A dramatic difference in the micro-pore distribution is observed in the two datasets derived from sample displaying ductile and brittle fracture. In the latter case the micro-pore distributions were interpreted to cluster near grain boundaries.

The presence of surface cracks in an inter-granularly failed sample of aluminum alloy pre-charged with hydrogen electrochemically seen in this study is common observation also reported by Gest, Toriano and several other researchers [47]. This feature is taken to be one of the important signatures of hydrogen embrittlement in aluminum alloys. This is because it was found that on grinding away the surface cracks there was improvement in ductility. Thus the embrittlement effects were considered to be two fold – one led by the surface cracks and the other due to hydrogen contained in the matrix inside. In both cases the inter-granular nature of failure through linking of cracked grain boundaries was found.

In the present work as the regions scanned using tomography are beneath the fracture surface it can be considered that the characteristics of damage in the respective datasets could be a snapshot that existed prior to final propagation of operating fracture mechanism across the tensile sample. The results of the quantitative tomography indicate that the transition to brittleness by hydrogen pre-exposure is accompanied by increase in both the micro-pore content as well as in the degree of its in-homogenous distribution within the matrix. Thus deforming a precharged Al-Zn-Mg-Cu alloy results in an increase in micro-pore levels even though the tendency for necking and fracture ductility levels are lower than the uncharged sample. This basic characteristic of the micro-damage architecture at failure, induced in this case by manifestation of hydrogen embrittlement is also seen in case of creep embrittlement in 9 – 12% Cr tempered martensitic steels [48]. It was shown in a 10%Cr heat resistant steel that long term creep at low stress near to 100 MPa results in an intergranular failure accompanied by an explosion of cavitation damage [48]. These similar features of two diverse embrittling phenomena point to a new feature in manifestation of embrittlement in materials, where the scale of damage development is divorced from influences of macroscopic plasticity and is governed by the relevant operating mechanisms of degradation.

In the present work the degradation effect which causes the brittle fracture in underaged Al-Zn-Mg-Cu is due to the presence of hydrogen in the deforming matrix. Even without

deformation the presence of elevated levels of hydrogen in aluminum alloys exacerbates damage [42]. It is well known that in aluminum alloys micro-pore development occur due precipitation of supersaturated hydrogen trapped in the matrix as a result of solubility gap in the solid and liquid states [49]. The ingress of hydrogen in pure aluminum, by the application of high fugacity electrochemical charging, results in an increase of matrix damage in the form of void and cracks [50]. Recent studies using thermal desorption spectrometry studies in hydrogen pre-exposed iron and steel show that plastic deformation after hydrogen pre-charging results in increase in matrix defect density [51]. The present work extends this relationship between hydrogen ingress and distribution, and increase in matrix damage by establishing that micro-pore architecture in the aluminum matrix intensifies inhomogenously prior to hydrogen induced intergranular fracture in underage AA7075. The ductile fracture displayed byAA7075 without precharging, on the other hand leads to the creation of micro-pore that is more homogenously distributed and tends to be near intermetallic particles suggesting that they originate from particle – matrix de-cohesion or particle cracking. Thus micro-pore architecture provides an imprint of the sites where damage intensifies due to the operating fracture mechanism. It is also of significance that these sites are also classed as deep hydrogen traps in high strength aluminum alloys, which makes the analysis relevant for the manifestation of hydrogen embrittlement.

In Al-Zn-Mg-Cu alloy a diverse range of trap sites exist that can accommodate elevated levels of hydrogen where degradation effect of hydrogen is likely to be manifested. These sites are lattice interstices, dislocations, vacancies, solute atoms, precipitates and high angle grain boundaries [26, 29]. Furthermore it has been shown by internal friction studies that solutes such as Cu or Mg are relatively weak traps [52] as their binding energies are lower than that of dislocations and high angle grain boundaries [40, 52]. The trapping tendency of hydrogen has been shown by the tritium autoradiography to be enhanced at dislocations introduced by cold work or at interfacial dislocations (eg. η/matrix interface) and repelled at GP zones with compressive stress fields [53, 54]. In a deforming aluminum matrix therefore the dislocations, and grain boundaries are likely serve as hydrogen trap sites. While strong experimental evidence supports the redistribution of hydrogen with dislocations during deformation, there is little evidence of preferential trapping at grain boundaries on hydrogen ingress from autoradiography studies in aluminum alloys. The capability of grain boundaries to trap internally supersaturated hydrogen has been shown by the application of TDS and micro-tomography to be more than the hydrogen micropores [26]. In the case of electrochemical precharging, however, steep gradients exist [55] that preclude the assumption that all

boundaries could be sufficiently enriched in hydrogen before deformation.

It is, however, evident from an intuitive reasoning that intergranular cracking cannot proceed without a grain boundary hydrogen enrichment step. While prior enrichment through simply precharging is questionable, it is more likely that it occurs in the hydrogen redistribution stage possibly by dislocations aided transport during deformation. Apart from dislocations, the appearance of vacancies (as shown in literature eg. [50]) and micro-pores (as shown in this work) during deformation in materials shows that the matrix dynamically increases the sites that are capable of accommodating hydrogen. Recent computational work carried out on Ni-H alloy system point to the fact that the increase in attendant matrix damage also increases hydrogen diffusivities provided high vacancy concentration prevails [56]. Such high concentration of vacancies can be found in regions of intense local plasticity [56, 57].

The redistribution of hydrogen to portent trap sites in Al-Zn-Mg-Cu is considered to be kinematically limited by the applied strain rate (eg. Tien et. al [58]), and must be therefore constrained by the concurrent processes that increase the diffusivity and the state of damage in the matrix. These are both controlled by the extent of localization of plasticity which is promoted by the presence of hydrogen. In the present work the results of the micro-pore clustering analysis on the dataset for the intergranularly failed samples can be interpreted as being near the grain boundaries. Considering that the grain boundaries are prominent sites for hydrogen redistribution in 7xxx alloys [26], the micro-pore agglomerations near boundaries could be rationalised in the following manner. The tensile deformation induces a non-uniform plastic strain within the matrix commensurate with the hydrogen distribution in the various traps. As the grain boundary hydrogen concentration is likely to be higher than the grain interior a localization of plasticity develops near the boundaries. Two factors sustain this effect – the kinetics of hydrogen redistribution and the presence of grain boundary cracks as a result of high fugacity charging. With continuing deformation the localized plasticity intensifies with increasing amount of hydrogen redistributing to the boundaries. Thus under the synergistic action of local hydrogen enrichment and intensification of plasticity that localizes dislocation motion into unshielded zones, damage in the form of micro-pores are likely to form. These micro-pores could further repartition the hydrogen, equilibrating its distribution within the matrix.

It is seen from the tomography dataset, however, that the matrix of the precharged AA 7075 after display of brittle fracture contains a number of internal cracks and a large surface connected intergranular cracks on the grain boundaries. The presence of large intergranular cracks could provide extended tri-axial field of influence that could destructively superimpose

on the governing influences of localized plasticity for micro-pore formation. Assuming that the most portent effect of crack tip field would be of the large crack a fracture mechanics analysis was carried out to show its expected region of influence rather than make an accurate estimation of the crack tip stresses. This analysis based on the slip line carried out by Yokobori et. al. [44, 45] was shown to result in accumulation of hydrogen near the elastic – plastic boundary. Others notably by Sofronis and McMeeking [46] point to the fact hydrogen concentration peaks at the point of maximum hydrostatic stress that lies at a distance of 1.53 times the crack tip opening displacement (CTOD). A first estimate of the CTOD is derived from the well-known relationship $\delta = K_I^2/\sigma_{ys}E$ (where δ = CTOD, E = Young Modulus, σ_{ys} = yield strength) and the distance of the maximum hydrostatic stress is calculated to be about 12μm for the present study where K_I = 17 MPa.m$^{1/2}$,σ_{ys} = 500 MPa and E = 71GPa (at 25ºC). As calculated from the equations 7 and 8, this distance of the maximum hydrostatic stress lies close to the elastic-plastic boundary at θ = 0°, where the stress is about $3\sigma_{ys}$. The expression for calculating the hydrostatic stress asymptotic component (σ_H(r)) assuming plane strain is given by $\sigma_H(r) = 2(1+\mu)K_I/3\sqrt{2\pi r}$ [45], where μ = Poisson ratio. At the elastic – plastic boundary at θ = 0°, (or r = 12μm from the crack tip), σ_H is $3.39\sigma_{ys}$. Thus both approaches place the value of the hydrostatic stress in the range 3 – $3.39\sigma_{ys}$ within the plastic zone of the intergranular crack tip, with the difference attributable to the presumed extent of constraint in deriving the expressions. In the present studies most of the micro-damage (> 80%) has been found to lie outside this plastic zone which implies that they are not influenced by hydrogen redistribution under the tri-axial stress field of the intergranular crack. It thus implies that crack tip plasticity does not govern the formation of micro-pore which strengthens the view that localized plasticity through inhomogenous strain distribution could lead to micro-pore agglomerated zones near grain boundaries.

Thus analysis of the micro-pore clusterings near the cracks provides the decisive indication of the microstructural origin of the spatial heterogeneity of the micro-damage architecture observed in the sample failed in ductile and brittle manner. The lack of systematic undulations in the β parameter for the uncharged dataset confirms that micro-pore are homogenously distributed and do not cluster near grain boundaries. It is evident from the coronal slices and composite overlay of intensity maps that the micro-pores in uncharged sample originate mostly near the intermetallic particles by particle matrix-de-cohesion or particle cracking. In contrast the origin of the heterogeneity of the micropore distribution in the intergranularly failed sample is related to their clustering near grain boundaries. The precharged AA 7075 subjected to tensile

deformation could be preferentially plasticized at grain boundaries due to their higher hydrogen content than the matrix. This could attract synergisms of hydrogen led strain localization and the ease of damage formation at sites of high hydrogen concentration to lead to the formation of micro-pore near the grain boundaries. It is to be pointed out that direct characterization of the incipient processes that lead to the formation of micro-pores near grain boundaries of hydrogen precharged Al-Zn-Mg-Cu requires techniques with sub-micrometer resolution and therefore is beyond the scope of the present work. However the evolution of micropore at intergranular cracks and strain localization tendencies in precharged Al-Zn-Mg-Cu alloy are within the realm of possibility using four dimensional techniques based on SR-μCT which is to be investigated in future.

5 Conclusions

1. The hydrogen pre-charging in underage AA7075 results in appearance of predominately intergranular mode of failure as compared to ductile failure in the uncharged sample.
2. The micro-damage architecture is significantly influenced by the intergranular mode of failure as compared to the ductile failure.
3. The micro-damage near surface connected intergranular crack in the pre-charged was composed of higher number of internal cracks and in-homogenously distributed micro-pores as compared with the region beneath the ductile fracture surface. The micro-pores content (volume fraction and number density) was larger in the dataset extracted from intergranularly failed sampled as compared with that of the sample failed in a ductile manner.
4. The majority of micro-pores in the sample failed in a brittle manner are not within the plastic zone of the large surface connected intergranular crack.
5. The origin of the in-homogenous micro-pore spatial distribution in the intergranularly failed sample is shown to be related to grain boundaries by the proximal analysis using image intensity maps and clustering analysis of a radial probability function.
6. The origin of the micro-pore spatial distribution in region beneath the ductile fracture surface is predominately governed by the particle matrix de-cohesion or particle cracking.
7. The origin of the inhomogenous micro-pore distribution near grain boundaries below the intergranular fracture surface is rationalized to be due to the synergistic action of local enrichment of hydrogen at the boundaries and the intensification of localized

plasticity.

Acknowledgements

CG gratefully acknowledges Japan Society for Promotion of Science (JSPS) for the JSPS fellowship award and the grant-in-aid for scientific research (No. 22.00384) that enabledthe research work to be carried out Toyohashi University of Technology. The synchrotron radiation experiments were performed with the approval of JASRI (Proposal No. 2011B1164). CG thankfully acknowledges all relevant staff at SPring-8, Japan for the support rendered during beam-time.

References

1. S P Lynch SP, Environmental assisted cracking : Overview of evidence for an adsorption – induced localised – slip process, Acta. Metall. 1988; 36: 2639.
2. R AOriani, Hydrogen – The versatile embrittler, Corrosion 1987; 43: 390 - 397.
3. Robertson IM, Lillig D, Ferreira PJ, Revealing the fundamental process controlling hydrogen embritlement in: Sonnerday. B, Sofronis P, Jones R (eds) Effects of hydrogen on Materials.
4. Gangloff RP, Hydrogen assisted cracking of high strength alloys in: Milne I, Ritchie RO, Karihalo O (eds) Comprehensive Structural Integrity Vol 6, New York :Elsevire Publishing, 2003.
5. G. A. Young Jr, J R Scully, The effects of test temperature, temper and alloyed copper on hydrogen controlled crack growth rate of an Al-Zn-Mg –(Cu) alloy, Metall. Mater. Trans., 33A (2002) 101 – 115.
6. I . M Robertson, H K Birnbaum, O Sofronis, Hydrogen effects in plasticity in: Hirth JP, Kubin L (eds) Dislocations in Solids, New York; Elsevier: 2009.
7. K Rajan, W. Wallace, J C Beddoes, Microstructural study of a high strength stress corrosion resistant 7075 aluminum alloy 17 (1982) 2817-2824.
8. T C Sai, T H Chuang, Role of grain size on the stress corrosion cracking of 7475 aluminum alloys, Mater. Sci. eng. A225 (1997) 135-144.
9. R K Viswanadham, T S Sun, J A S Green, Grain boundary segregation in Al-Zn-Mg alloys – implications to stress corrosion cracking, Metall. Trans 11A (1980) 85-89.
10. L Christodoulou, H M Flower, Hydrogen embrittlement and trapping of Al-6%Zn-3%Mg,Acta. Metall., 28 (1980) 481- 487.

11. P K Poulose, J E Morall, A J McEvily, Stress corrosion crack velocity and grain boundary precipitates in an Al-Zn-Mg alloy, Metall. Trans. 5A (1974) 1393-1400.
12. G M Scamans, H J H Holroyd, C D S Tuck, The role of magnesium segregation in the intergranular corrosion cracking of aluminum alloys Corros. Sci. 1987; 27: 329.
13. Hyatt MV, Spiedel MO, High Strength aluminum alloys in: Stahele RW (eds) Advances in corrosion science and technology vol 2 New York: Plenum Press ; 1972.
14. J Albrecht, A W Thompson, I M Bernstein, The role of microstructure in hydrogen assisted fracture of 7075 aluminum, Metall. Trans. 10A (1979) 1759-1766.
15. Najjar D, Magnin T, Warner T, Influence of critical surface defects and localised competition between anodic dissolution and hydrogen effects during stress corrosion cracking of a 7050 aluminum alloy, Mater. Sci. Eng. 238A (1997) 293-302.
16. H K Birnbaum, C Buckely, F Zeides, E Sirois, P Rozenak, S Spooner, J S Lin, Hydrogen in aluminum, Jour. Alloy. Comp. 253-254 (1997) 260-264.
17. P Rozenak, Defects producing formation of micro-cracks in aluminum during electrochemical charging with hydrogen, Jour. Alloy. Comp., 400 (2005) 106-111.
18. F Eckermann, T Suter, P J Uggowitzer, A Afseth, A J Davenport. B J Connoly, M H Larsen, F De Carlo, P Schmutz, In-situ monitoring of corrosion process within bulk of AlMgSi alloys using X-ray microtomography, Corros. Sci. 50 (2008) 3455 – 3566.
19. B J Conolly, B A Horner, S J Fox, A J Davenport, C Padovani, S Zhou, A Turnbull, M Preuss, N P Stevens, J J Marrow, J –Y Buffiere, E Boller, A Groso, M Stampanoni, X-ray microtomography studies of localized corrosion and transitions to stress corrosion cracking, Mat. Sci. Tech. 22 (2006) 1076 – 1085.
20. S P Knight, M Salagaras, A M Wythe, F De Carlo, A J Davenport, A R Trueman, In-situ X-ray tomography of intergranular corrosion of 2024 and 7050 aluminum alloys, Corros. Sci. 52 (2010) 3855 – 3860.
21. S M Gharari, A J Davenport, T Raymend, T Suter, J –P Tinnes, C Padovani, J A Hammons, M Stampanoni, F Marone, R Mokso, In-situ synchrotron X-ray microtomography study of pitting corrosion in stainless steel, Corros. Sci. 53 (2011) 2684 – 2687.
22. S S Singh, J J Williams, M F Lin, X. Xiao, F De Carlo, N Chawla, In situ investigation of high humidity stress corrosion cracking of 7075 aluminum alloy by three-dimensional (3D) X-ray synchrotron tomography, Materials Research Letters, 2 (2014) 217-220.
23. S S Singh, J J Williams, T J Stannard, X Xiao, F De Carlo, N Chawla,. Measurement of Localized Corrosion Rates at Inclusion Particles in AA7075 by In Situ Three Dimensional (3D) X-ray Synchrotron Tomography Corros. Sci., 104 (2016) 330-335.

24. S S Singh, J J Williams, P Hruby, X Xiao, F De Carlo, N Chawla, “In situ experimental techniques to study the mechanical behavior of materials using X-ray synchrotron tomography”, Integrating Materials and Manufacturing Innovation, 3 (2014) 1-14.
25. S. S. Singh, C Schwartzstein, J J Williams, X Xiao, F De Carlo, N Chawla, 3D microstructural characterization and mechanical properties of constituent particles in Al 7075 alloys using X-ray synchrotron tomography and nanoindentation, Jour. Alloys. Comp. 602 (2014) 163-174.
26. A Griesche, E Dabah, TKannengiesser, N Kardjilov,AHilger, I Manke, Three-dimensional imaging of hydrogen blister in iron with neutron tomography, Acta. Mater. 78 (2014) 14-22.
27. T Hoshihira, T Otsuka, T Tanabe, Visualisation of hydrogen distribution around blisters by tritium radio-luminography, J. Nucl. Mater. 386-88 (2009) 776-779.
28. Md. S. Bhuiyan, H. Toda, Z. Peng, S. Hang, K. Horikawa, K. Uesugi, A. Takeuchi, N. Sakaguchi, Y. Watanabe, Mater. Sci. Eng. 655A (2016) 221 – 228.
29. G A Young Jr, J R Scully, Acta. Mater., The diffusion and trapping of hydrogen in high purity aluminum, 46(1998) 6337-6349.
30. Asano S, R Otsuka, The lattice hardening due to dissolved hydrogen in iron and steel, Scripta Metall. 1976; 10: 1015 - 1020.
31. Maire E, Withers P J, Quantitative Tomography, Inter. Mater. Rev. 2014; 59: 1 - 49.
32. Burnett T L, McDonald S A, Ghlina A, Geurts R, Slater T, Haigh S J, Ornek C, Almualli F, Engelberg D L, Thompson G E, Wither P J, Correlative Tomography Sci. Rep. 2014; 4: 04711.
33. Gupta C, Toda H, Mayr P, Sommitsch C, Cavitation studies in materials : New insights from modern techniques in 2D/3D/4D characterisation Mater. Sci. Tech. 2015; 31: 513 - 515.
34. G M Scamans, Discontinuous propagation of stress corrosion cracks in Al-Zn-Mg alloys, Scr. Metall. 1979; 13: 245-251.
35. A Takeuchi, K Uesugi, H Takano, Y Suzuki, Sub-micrometre resolution three dimensional imaging with hard X-ray imaging microtomography, Rev. Sci. Instrum., 2002; 73: 4246-4250.
36. D Seo, F Tomizato, H Toda, K Uesugi, A Takeuchi, Y Suzuki, M Kobayashi, Spatial resolution of synchrotron x-ray microtomography in high energy range : Effect of x-ray energy and sample to detector distance, Appl. Phys. Lett. 101 261901 (2012).
37. J J Williams, Z Flom, A AAmell, N Chawla, X Xiao, F De Carlo, Damage evolution in SiC

particle reinforced alloy matrix composites by X-ray synchrotron tomography, Acta. Mater. 58 (2010) 6194 – 6205.

38. X. Zang, M Guo, J Zhang, L Zhang, Dissolution of precipitates during solution treatment of Al-Mg-Si-Cu alloys, Metall. Mater. Trans. 47B (2016) 608 – 620.
39. D Nguyen, A W Thompson, I M Bernstein, Microstructural effects on hydrogen embrittlement in a high purity 7075 aluminum alloy, Acta. Mater. 35 (1987) 2417-2425.
40. H Toda, T Hidaka, M Kobayashi, K Uesugi, ATakeuchi, K Horikawa. Growth behavior of hydrogen micropores in aluminum alloys during high-temperature exposure, Acta. Mater. 57 (2009) 2277-2290.
41. H Toda, K Minami, K Koyama, K Ichitani, M Kobayashi, K. Uesugi, Y. Suzuki, Healing behavior of preexisting hydrogen micropores in aluminum alloys during plastic deformation, Acta. Mater. 57 (2009) 4391-4403.
42. C. Gupta, H. Toda, T. Fujioka, M. Kobayashi, K. Uesugi, A. Takeuchi, Y. Suzuki, Micro-pore development phenomenon in hydrogen pre-charged aluminum alloy studied using synchrotron X-ray microtomography, Appl. Phys. Lett. 103 171902 (2013).
43. C. Gupta, H Toda, T. Fujioka, M. Kobayashi, H. Hoshino, K. Uesugi, A. Takeuchi, Y. Suzuki, Corros. Sci. (2016) Accepted for publication doi:10.1016/j.corsci.2016.04.050 .
44. A T Yokobori Jr, Y Chinda, T Nemoto, K Satoh, T Yamada, The characteristics of hydrogen diffusion and concentration around a crack tip concerned with hydrogen embrittlementCorros. Sci., 44 (2002) 407-424.
45. A T YokoboriJr, T Nemoto, K SatohK, T Yamada, Numerical analysis on hydrogen diffusion and concentration in solid with emission around the crack tip, Eng. Fract. Mech. 55 (1996) 47-60.
46. P Sofronis, R M McMeeking, Numerical analysis of hydrogen transport near a blunting crack tip, J. Mech. Phys. Solids 37 (1989) 317-350.
47. R J Gest, A R Toriano, Stress corrosion and hydrogen embrittlement in an aluminum alloy Corrosion, 1974; 30: 274-279.
48. C. Gupta, H. Toda, C. Schlacher, Y. Adachi, P. Mayr, C. Sommitsch, K Uesugi, Y. Suzuki, A. Takeuchi, Study of creep cavitation behavior in a tempered martensitic steel using synchrotron micro-tomography and serial sectioning techniques, Mater. Sci. Eng. 564A (2013) 525 – 538.
49. D.E.J. Talbott, Effects of hydrogen in aluminum, copper and their alloys, Int. Metall. Rev. 20 (1975) 166 – 184.
50. P Rozenak, States of hydrogen and deuterium in chemically charged high purity

aluminumJour. Alloy. Comp., 587 (2014) 800 - 806.

51. K. Takai, H. Shoda, H. Suzuki, M. Nagumo, Lattice defects dominating hydrogen related failures of metalsActa. Mater. 56 (2008) 5158 – 5167.
52. M. Leger, G R Piercy, Internal friction of hydrogen charged aluminum alloys, Phil. Mag, 43A, (1981) 377-385.
53. H Saitoh, Y Ijima, K Hirano, Behavior of hydrogen in pure aluminum, Al – 4 mass % Cu and Al-1 mass % Mg_2Si alloys studied by tritium autoradiagraphy, Jour. Mat. Sci. 29 (1994) 5739 – 5743.
54. Y Iijima, S -I Yoshida, H Saitoh, H Tanaka, K –I Hirano, Hydrogen trapping and repelling in an Al-6%Zn-2%Mg, J. Mat. Sci., 27 (1992) 5735-5738.
55. J. T. Burns, R. P. Gangloff,Effect of low temperature on fatigue crack formation and microstructure scale growth from corrosion damage in Al-Zn-Mg-Cu, Metall. Mater. Trans. 44A(2013) 2083-2105.
56. Y. Wang, D. Connétable, D. Tanguy, Influence of trap connectivity on H diffusion : Vacancy Trapping, Acta. Mater. 103 (2016) 334-340.
57. D. Setman, E. Schafler, E. Korznikova, M. J. Zehetbauer, The presence and nature of vacancy type defects in nanometals detained by severe plastic deformation, Mater. Sci. Eng. 493A (2008) 116-112.
58. J K Tien, A. W. Thompson, I. m. Bernstein, R. J. Richards, Hydrogen transport by dislocations, Metall. Trans. 7A (1976) 821 - 829.

Table 1: Chemical composition of the AA 7075 used for the investigations

Si	Fe	Cu	Mn	Mg	Cr	Zn	Ti	Zr+Ti	Al
<0.40	<0.50	1.6	<0.30	2.5	0.23	5.6	<0.20	<0.25	bal.

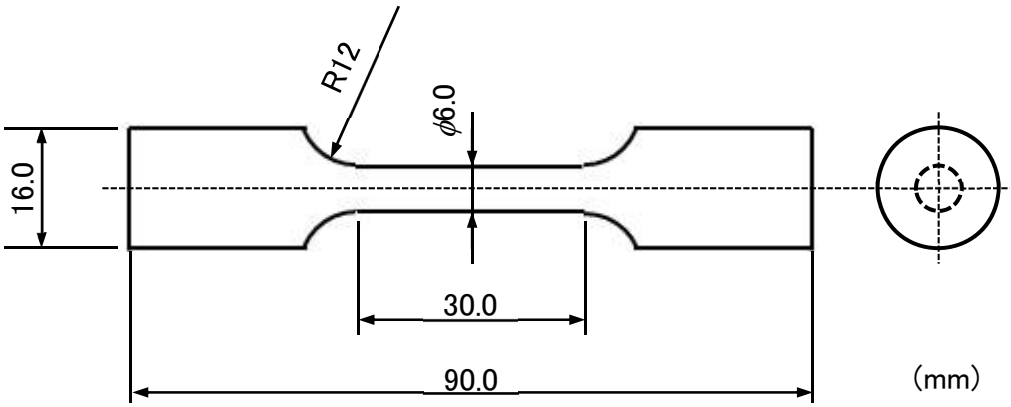

Figure 1 Schematic of the cylindrical tensile specimen used for the studies

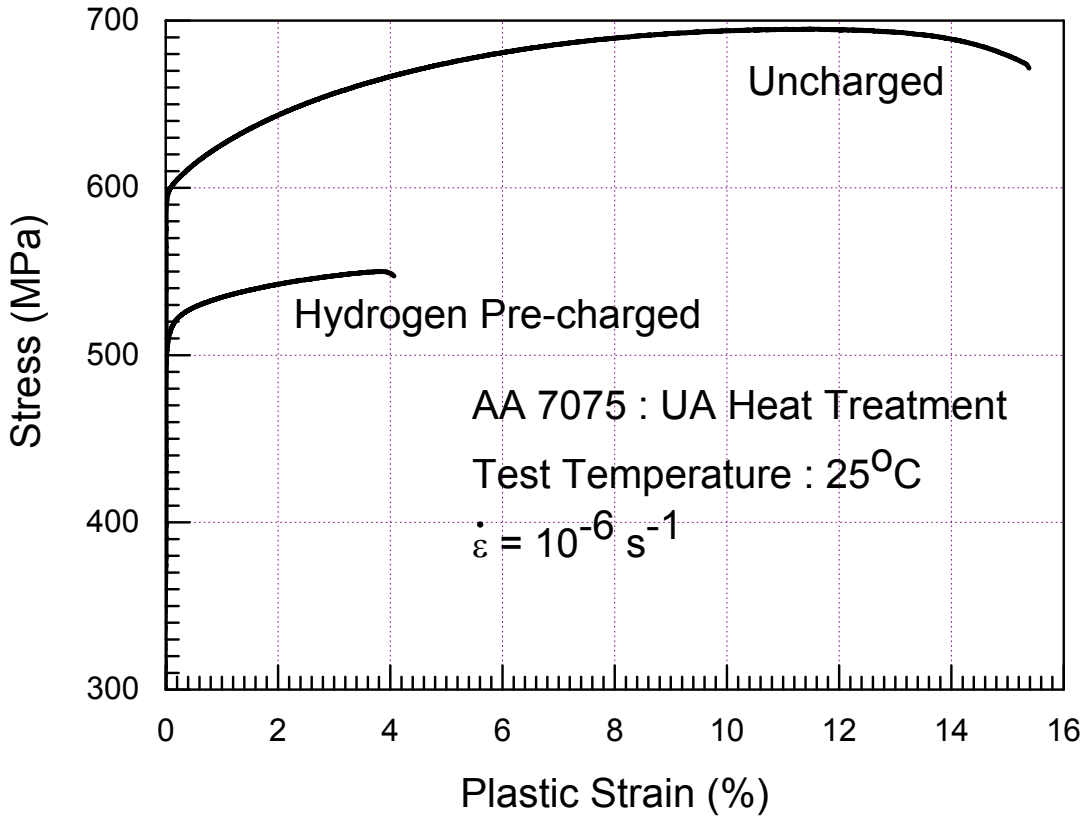

Figure 2. Plot showing the comparison of flow curve of hydrogen pre-charged and uncharged AA 7075 UA material tested at room temperature at strain rate of 10^{-6} s^{-1}.

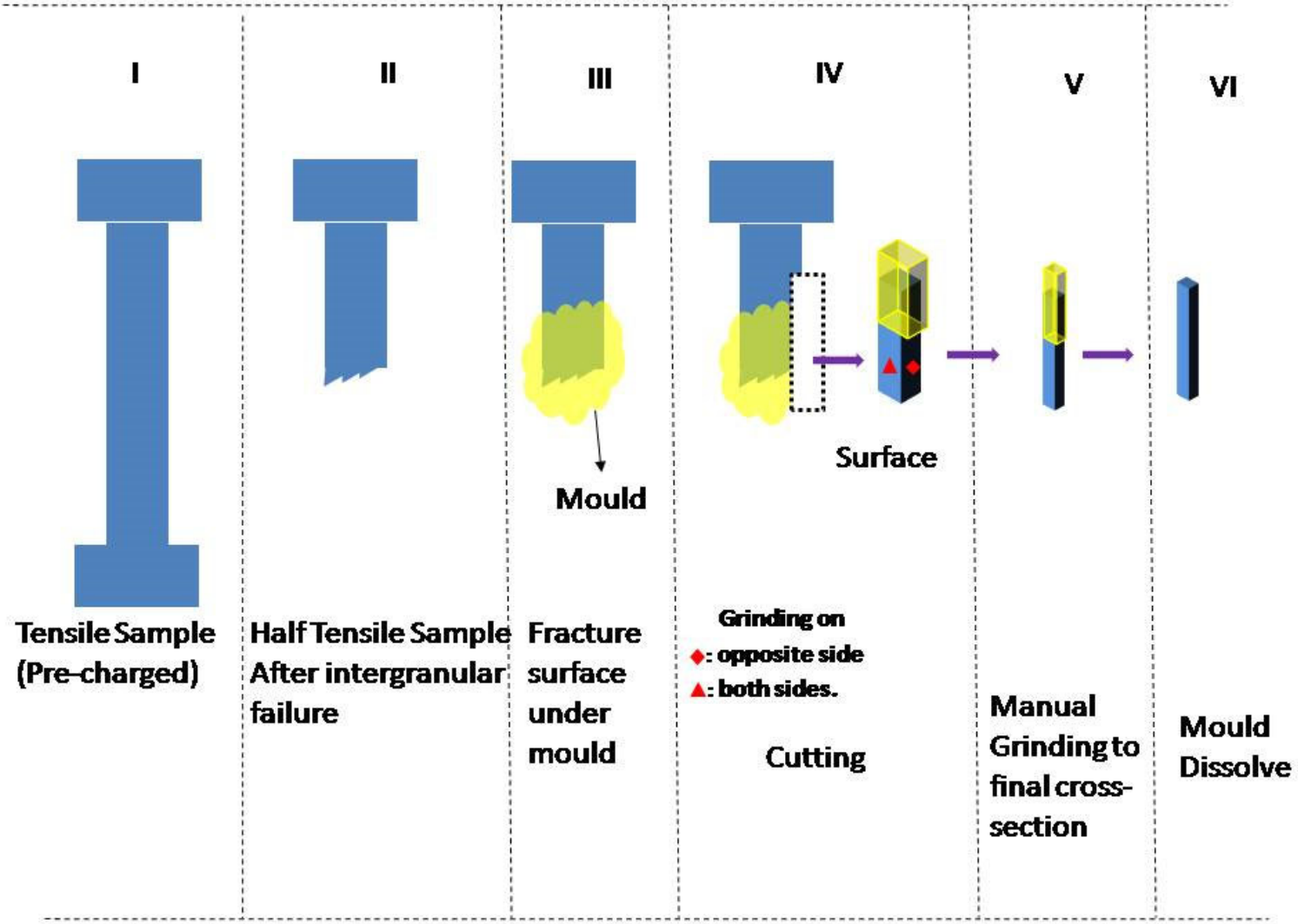

Figure 3 A schematic depicting the sequential stages in the extraction of sample coupon from failed tensile tested sample and its preparation for microtomography scanning.

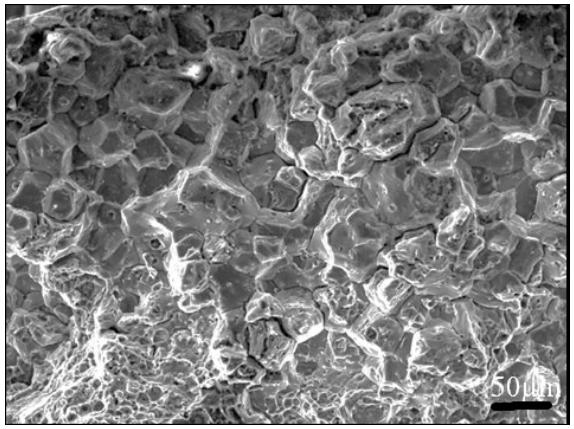

(a)

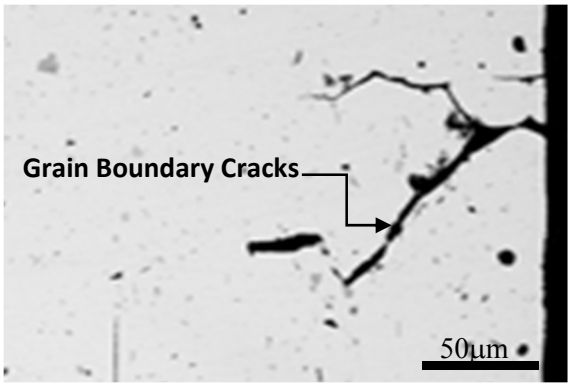

(b)

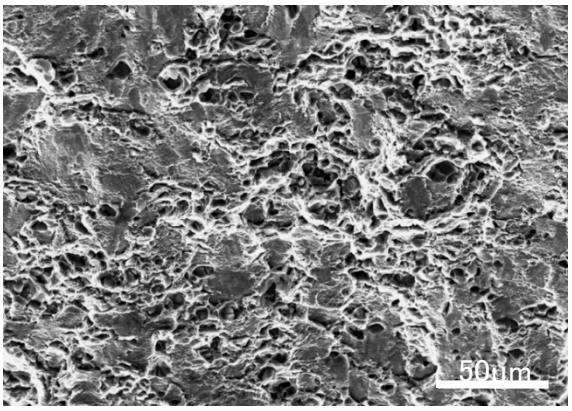

(c)

Figure 4: (a) SEM fractograph showing the intergranular failure of the pre-charged tensile sample. (b) Optical micrograph near the outer surface of the intergranularly failed tensile sample showing the presence of surface connected intergranular cracks. (c) SEM fractograph showing ductile failure of the uncharged tensile sample of underaged AA7075.

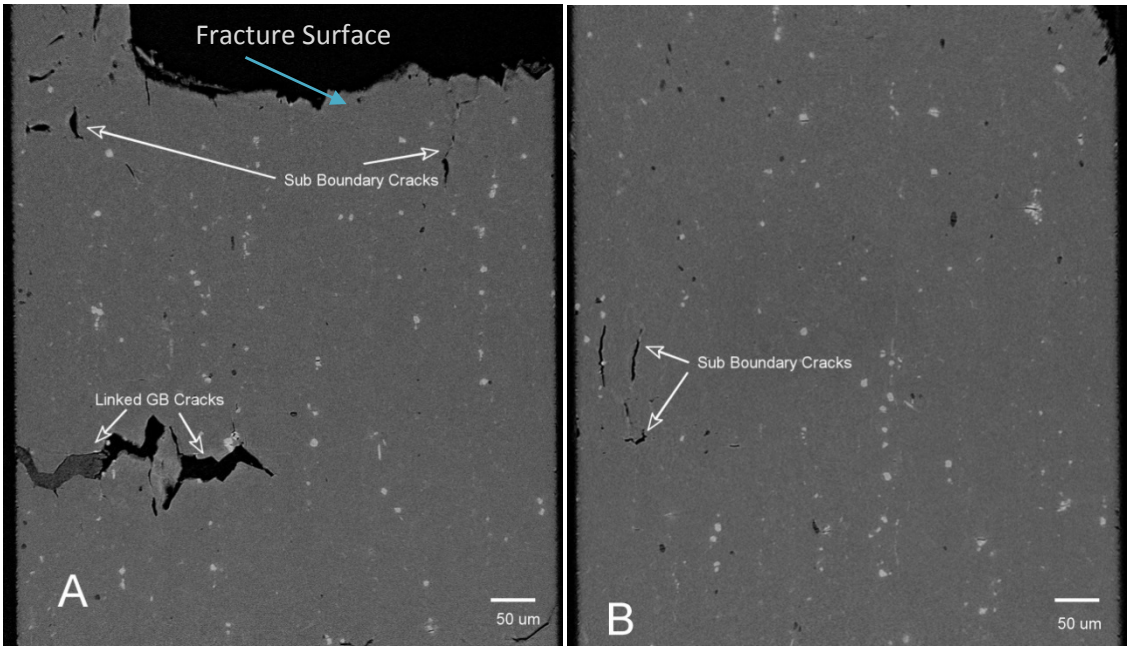

(a) (b)

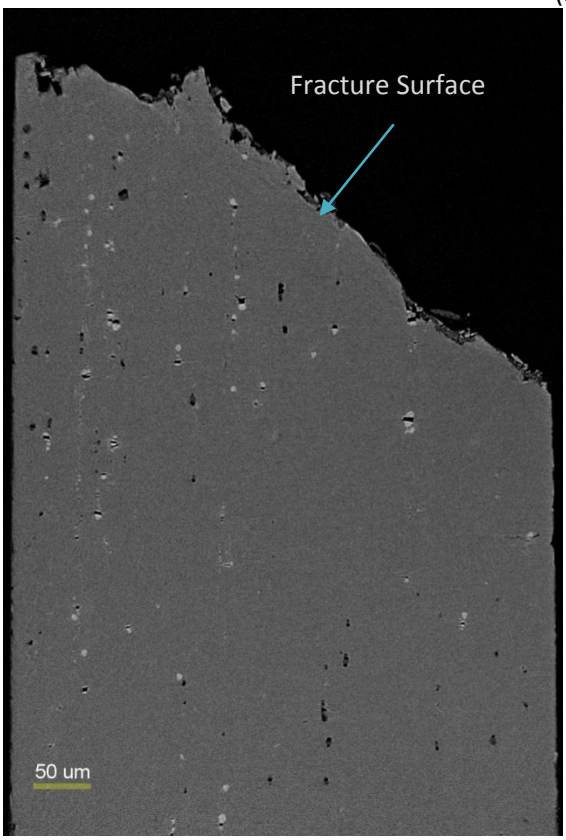

(c)

Figure 5 Coronal slice from SR-µCT showing Al matrix as gray, damage as black and Fe-Mg-Cu intermetallic particles as bright spots in (a) region A (b) region B of charged sample coupon dataset (c) sample coupon of Uncharged dataset.

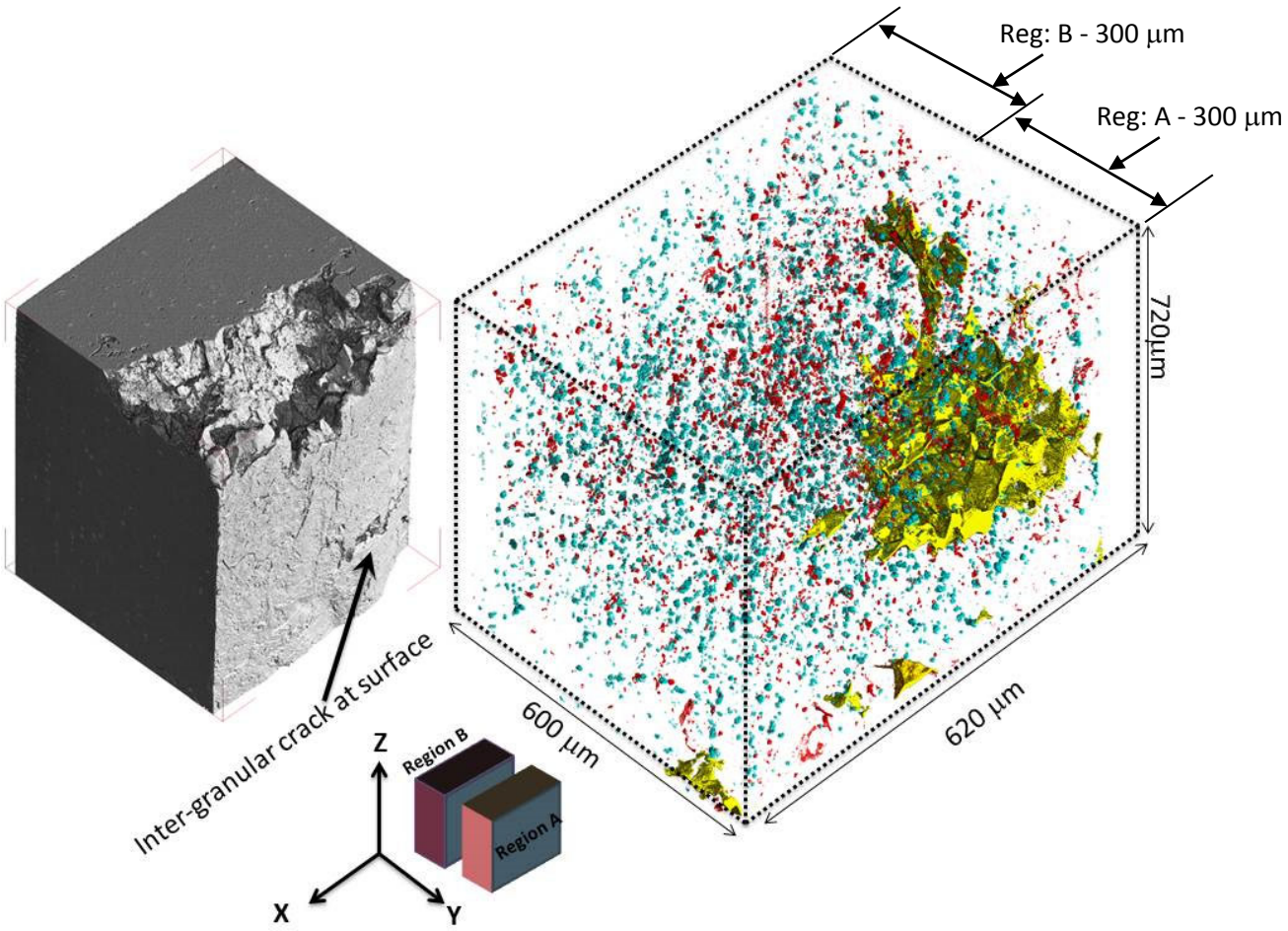
Reg: B - 300 µm
Reg: A - 300 µm
720µm
600 µm
620 µm
Inter-granular crack at surface
Z
Region B
Region A
X
Y

(a)

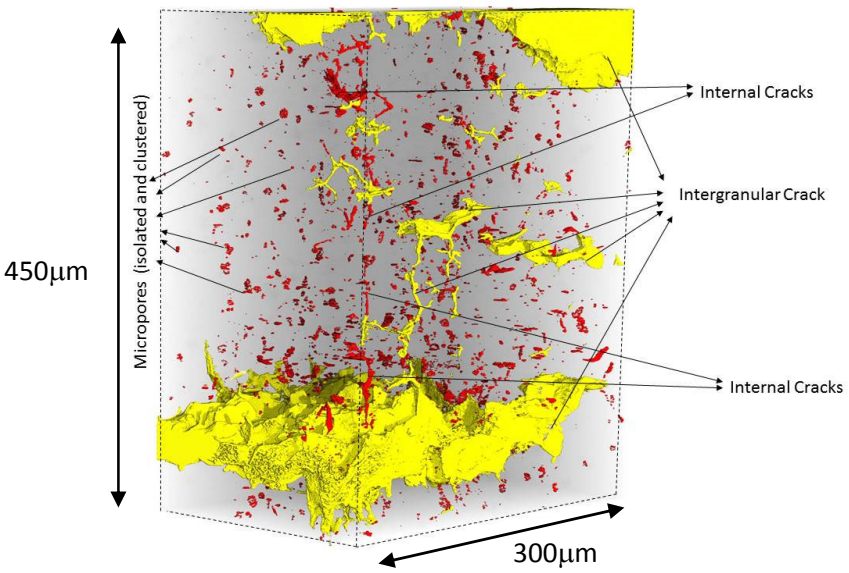
450µm
Micropores (isolated and clustered)
Internal Cracks
Intergranular Crack
Internal Cracks
300µm

(b)

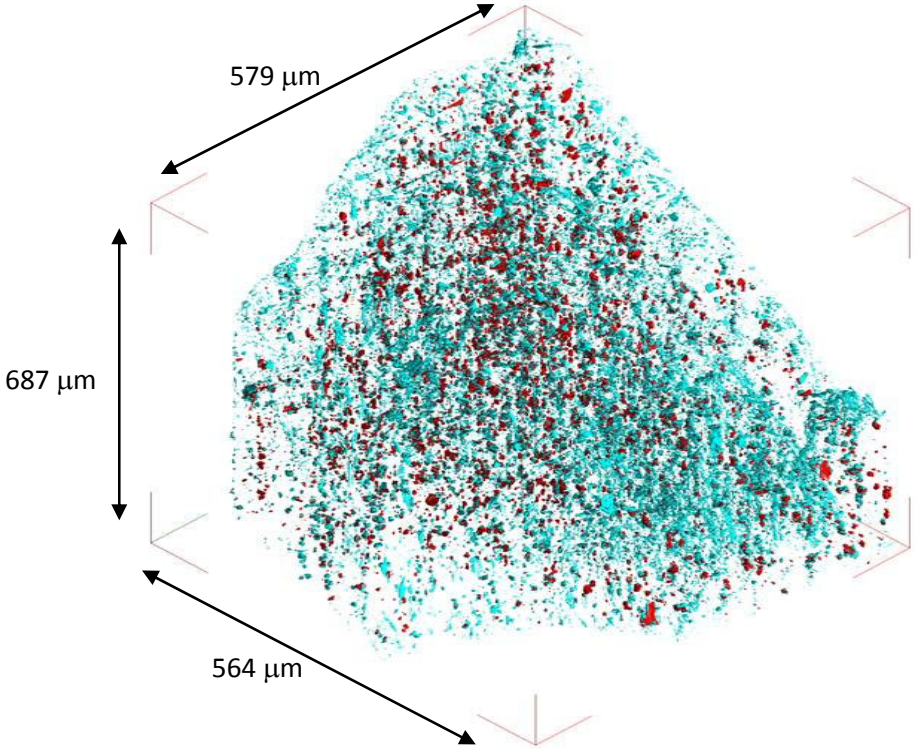

(c)

Figure 6.(a) 3D visualization of the volume scanned using microtomography showing the surface and the internal scanned volume of the charged dataset containing particles (aqua), pores/voids (red) and cracks (yellow). The two regions where the quantitative and spatial intensity maps have been compared are also shown. (b) 3D visualization of the volume showing the various form of micro-damage near to the intergranular crack of the charged dataset.(c) 3D rendering of the volume scanned by SR-µCT containing the fracture surface showing the pores (red colour) and particles (aqua colour) of the uncharged dataset.

Table 2: 3D characteristics of the micro-damage and particles in the sub-datasets: region A & B, and uncharged sample.

3D Parameter	Micro-damage			Particle		
	Reg. A	Reg. B	Uncharged	Reg. A	Reg. B	Uncharged
Volume Fraction (%)	0.528	0.11	0.18	0.22	0.23	0.143
Number Density /m^3 10^{12}	36.31	27.56	34.36	51.46	47.93	69.58
Size(μm) ($\bar{d} \pm 1\sigma$)	3.46±2.7	3.33±1.49	3.43±1.89	3.58±1.69	3.77±1.7	3.01±1.08
Sphericity ($\bar{S} \pm 1\sigma$)	0.25±0.14	0.24±0.15	0.38±0.16	0.20±0.13	0.21±0.14	0.26±0.14
Inter – object distance (μm)	301	331	307	268	275	243

$\bar{d}$ = Average Size ;σ = standard distribution ; $\bar{S}$ = Sphericity

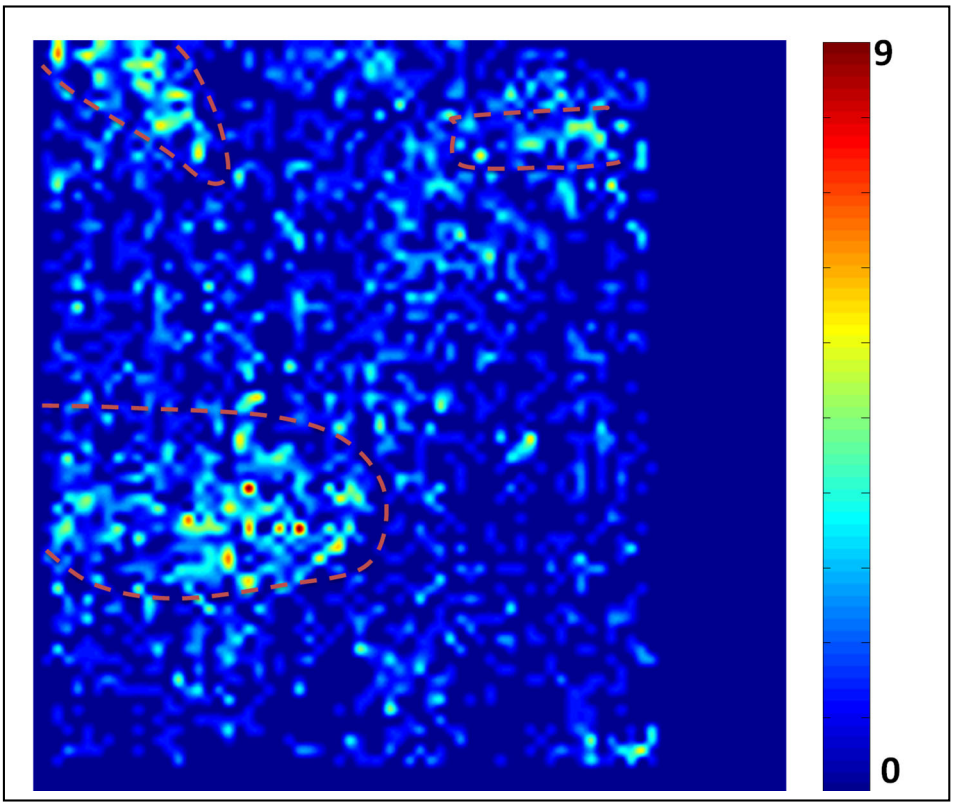

(a)

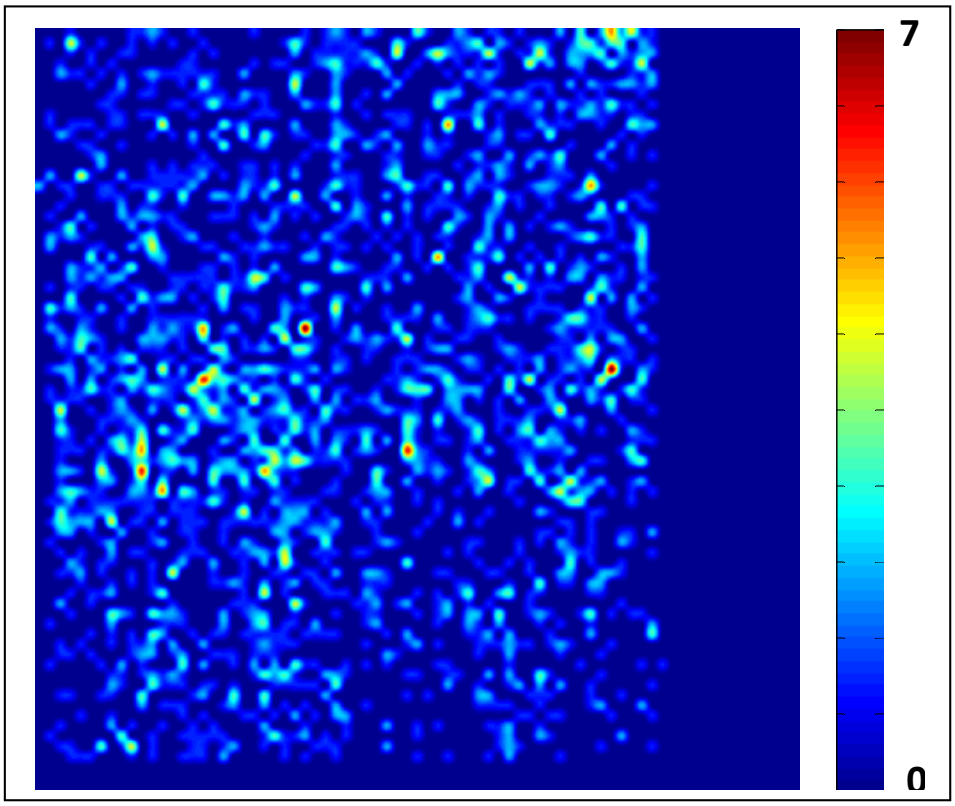

(b)

Figure 7. The spatial distribution of pores in sub-volume depicted as image intensity maps in the (a) region A with sub-volume dimension 20x20x210 μm^3, (b) region B with sub-volume dimension 20x20x240 μm^3.

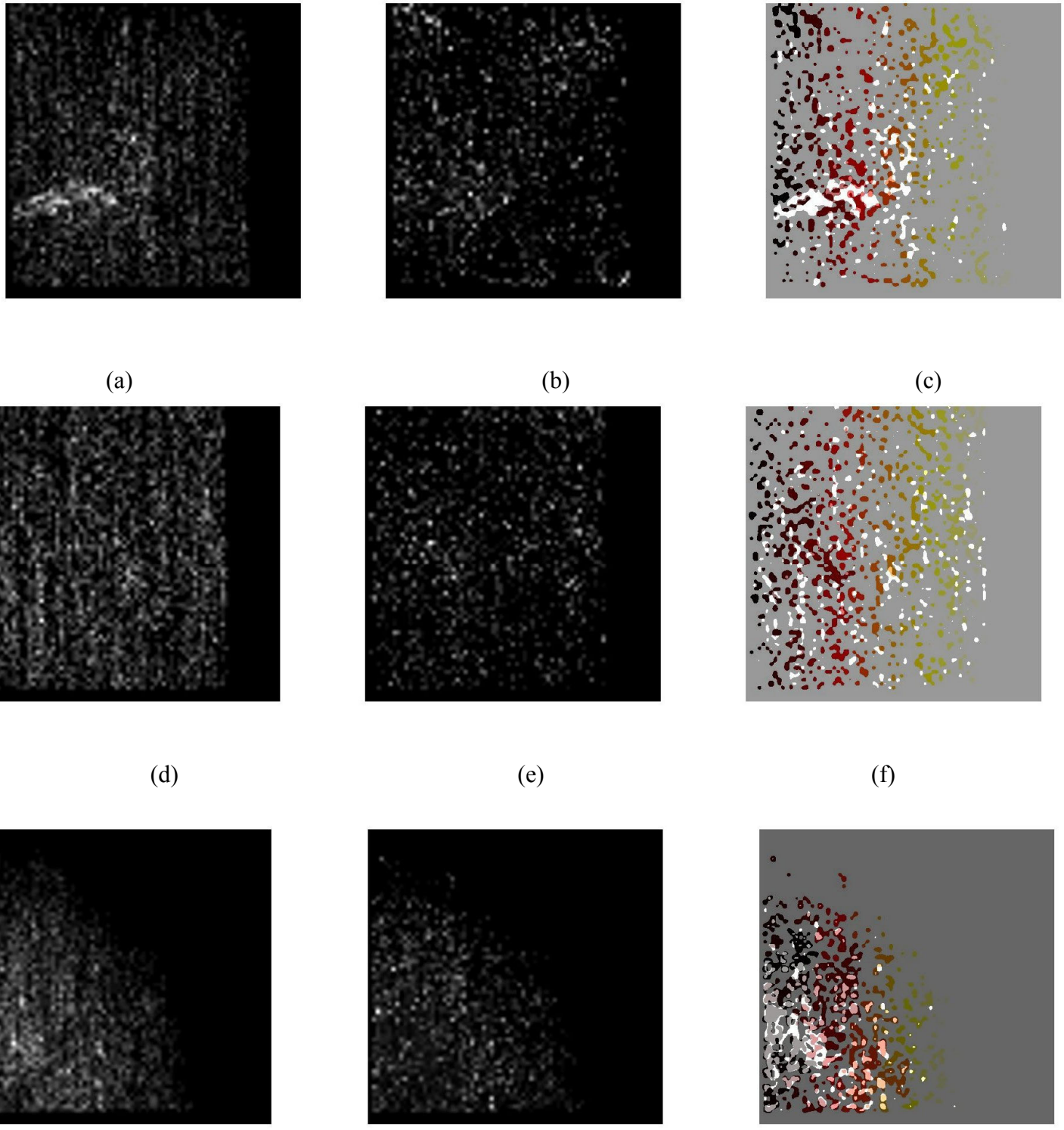

Figure 8. Images obtained by depicting the spatial intensity map of the dataset of region A (a) particles (b) γ - parameter (c) “Composite” image of (a) & (b); Images obtained by depicting the spatial intensity map of the dataset of region B (d) particles (e) γ - parameter (f) “Composite” image of (d) & (e); Images obtained by depicting the spatial intensity map of the dataset for uncharged sample(g) particles (h) γ - parameter (i) “Composite” image of (g) & (h)

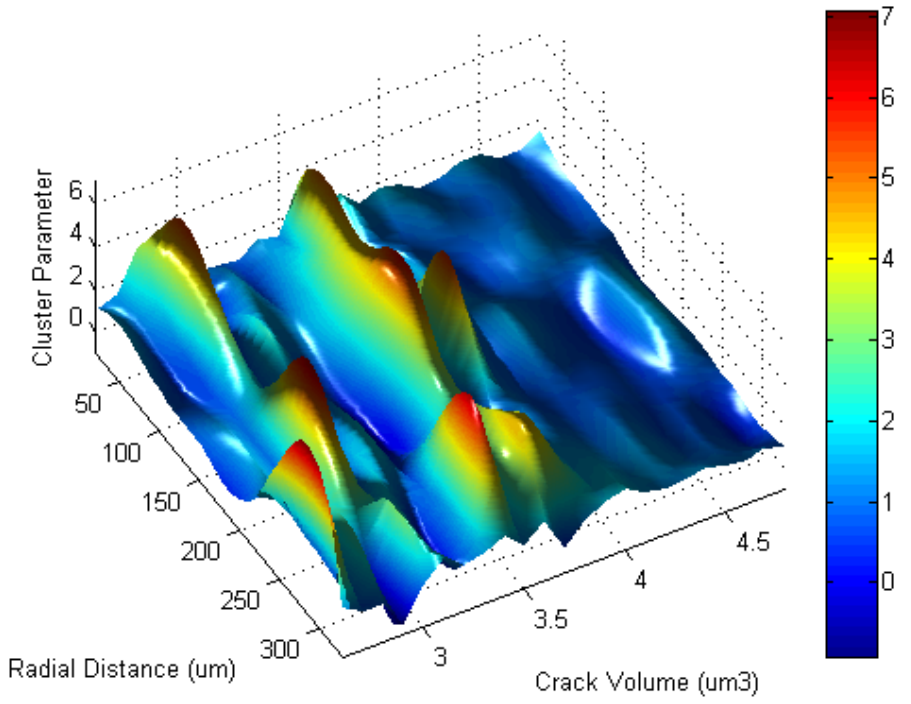

(a)

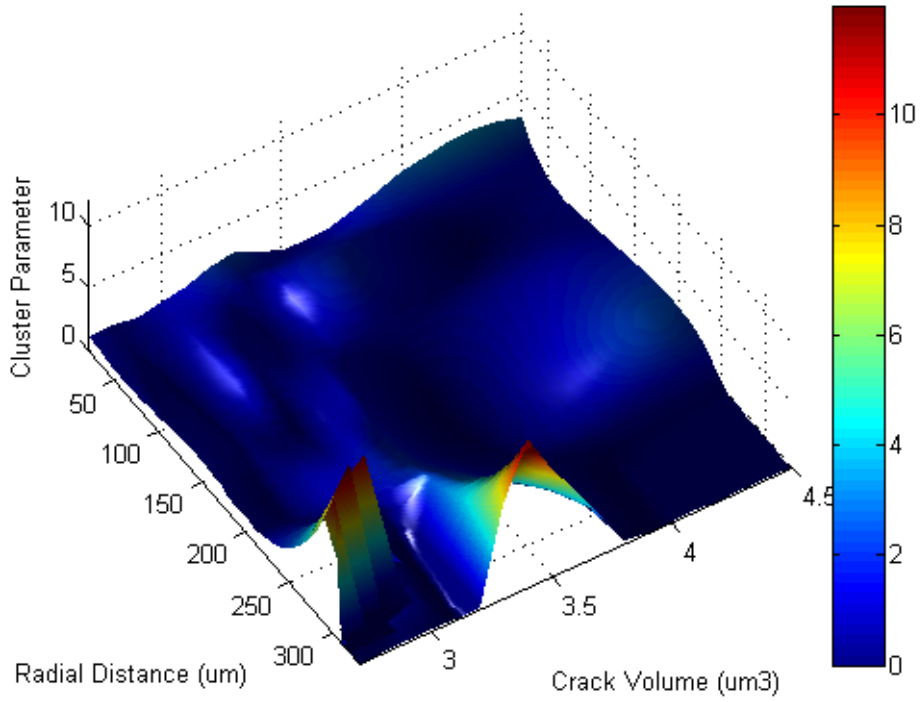

(b)

Figure 9 3D surface plot of the peak clustering of a radial proximity function as a function of radial distance from intergranular cracks and pore volumes in (a) region A (b) region B.

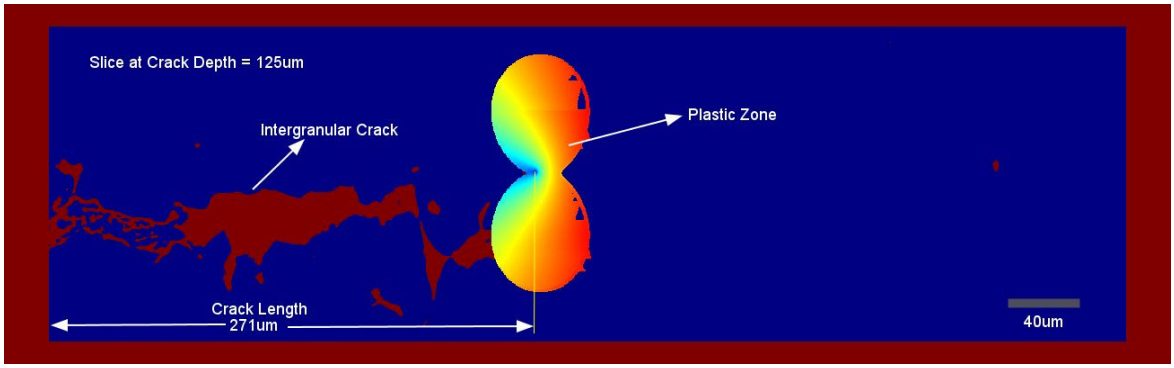

Figure 10. An enlarged view of the coronal slice containing the intergranular crack at a depth of 125µm from the surface showing the extent of the plastic zone size at the crack tip.

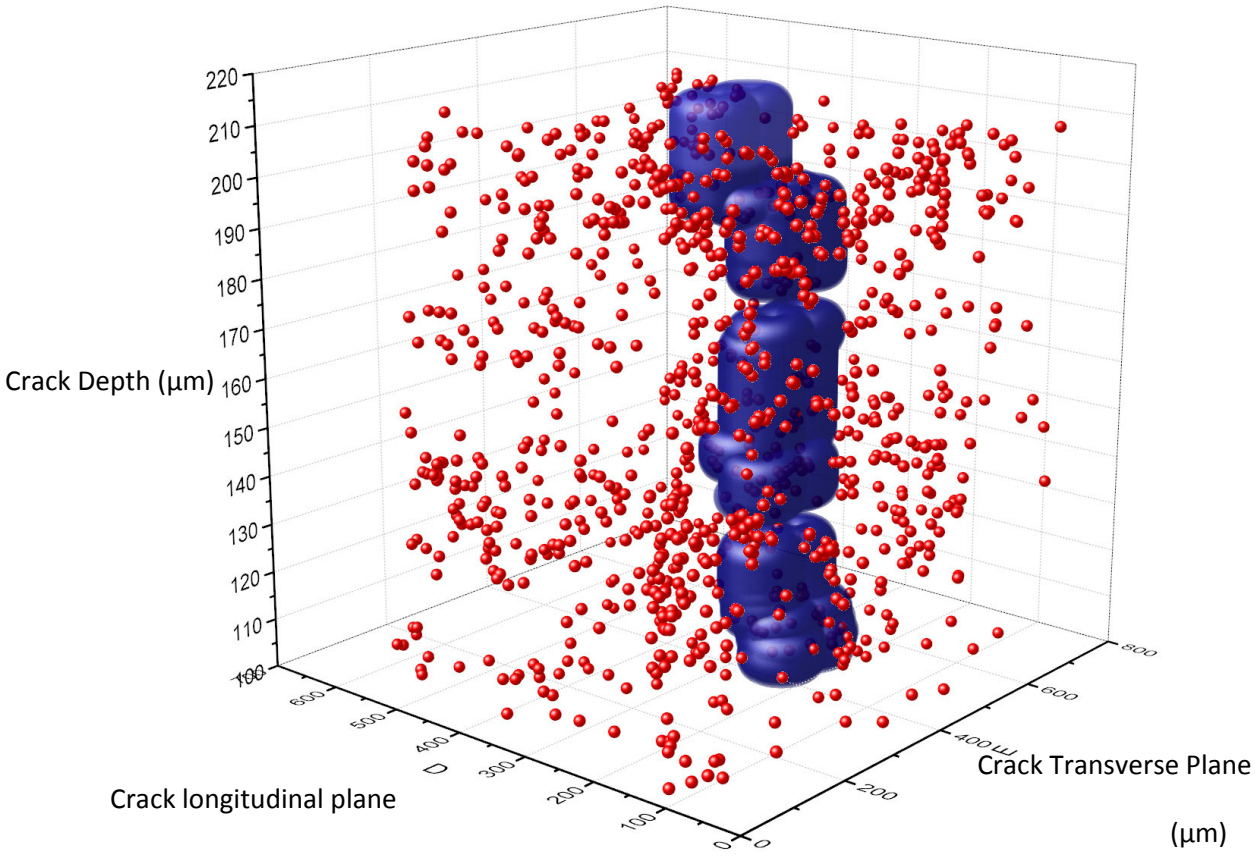

Figure 11. A 3D scatter plot showing the proximal relationship of the micro-pore (red) location with the plastic zone size (blue).

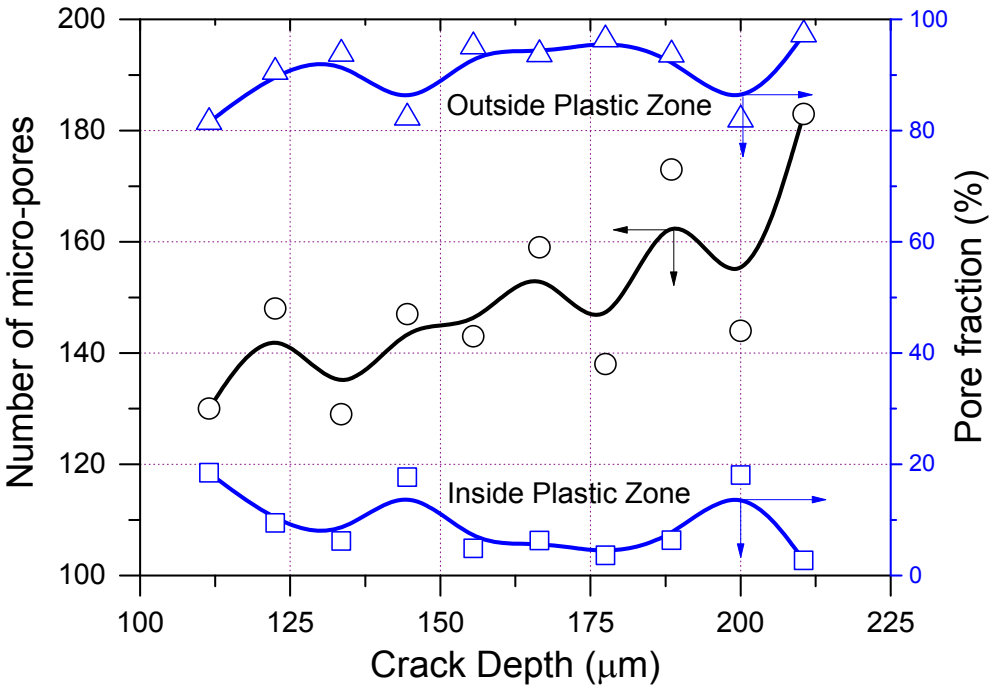

(a)

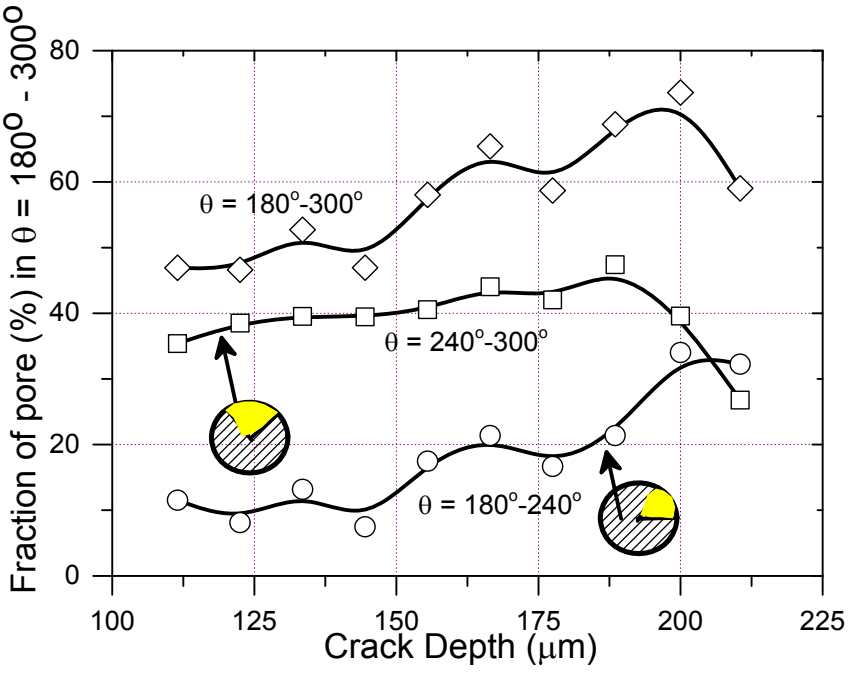

(b)

Figure 12 (a) Plot of distribution of the micro-pore inside and outside the plastic zone (b) Plot of the fraction of the pore in the prescribe direction to the crack tip.